Compact Inverse-Opal Electrode Using Non-Aggregated TiO_2 Nanoparticles for Dye-Sensitized Solar Cells

By *Eun Sik Kwak, Wonmok Lee, Nam-Gyu Park, Junkyung Kim,* and *Hyunjung Lee**

Compact inverse-opal structures are constructed using non-aggregated TiO_2 nanoparticles in a three-dimensional colloidal array template as the photoelectrode of a dye-sensitized solar cell. Organic-layer-coated titania nanoparticles show an enhanced infiltration and a compact packing within the 3D array. Subsequent thermal decomposition to remove the organic template followed by impregnation with N-719 dye results in excellent inverse-opal photoelectrodes with a photo-conversion efficiency as high as 3.47% under air mass 1.5 illumination. This colloidal-template approach using non-aggregated nanoparticles provides a simple and versatile way to produce efficient inverse-opal structures with the ability to control parameters such as cavity diameter and film thickness.

1. Introduction

Dye-sensitized solar cells (DSSCs)[1] are regarded as a regenerative low-cost alternative to conventional solid-state energy conversion devices using random network TiO_2 films. In order to generate a high photocurrent within the cells, the TiO_2 electrode in DSSCs demands high porosity and surface area so that the sensitizers can be sufficiently adsorbed and the paths for electron transport can be electronically interconnected.[2–4]

Conventional TiO_2 anodes have typically been prepared through the deposition of TiO_2-nanoparticle-based polymer pastes by screen printing and sintered to produce electrically continuous paths. In this structure, a key issue has been to enhance the dispersion of the TiO_2 nanoparticles in the solvent or polymer matrix to provide sufficient electron conducting paths and high surface area for dye adsorption. In addition, the disordered geometrical structures in nanoparticle-based DSSCs are limiting factors for achieving higher efficiency due to interfacial interference for electron transport.[5–12] The trap-limited diffusion process in randomly connected networks can be disturbed by recombination with the oxidizing species in the electrolyte during a number of trapping steps.[3,13,14]

In conjunction with these efforts, recent studies on photoelectrodes have expanded the processing strategies by using periodic nanostructures with long-range ordering to better assure an interconnected morphology of the TiO_2 structure. Such periodic structures have shown promising results for wide bandgap semiconductor materials,[15–21] core–shell structures,[22,23] nanowire (nanotube) structures,[6–11,24–26] and inverse-opal (IO) structures.[27–33] In particular, ordered IO structures of two-dimensional or three-dimensional (2D or 3D) colloidal crystals have been successfully utilized in the modification of the absorption bands of dye sensitizers due to the photonic bandgap effect in DSSCs.[30–33] There are several challenging issues in obtaining a high-quality IO structure (i.e., complete infiltration of the pores with the desired materials and minimization of the volume shrinkage-induced cracks in IO structures).[34–39] So far, TiO_2 inverse-opal structures for solar cells have been prepared primarily through sol–gel hydrolysis of metal alkoxide precursors such as titanium(IV) tetra-isopropoxide or titanium *n*-butoxide. The difficulties lie in making thicker (>5 μm) self-assembled layers and dense filling of the TiO_2 particles between the colloidal particles, which limit the performance of IO-structured DSSCs.

To satisfy these requirements for efficient electron transport, here a novel approach for fabricating IO structures with non-aggregated TiO_2 nanoparticles on a conducting glass substrate is described. The TiO_2 nanoparticles used in this study were protected from aggregation through the existence of outer organic layers.[40] The fabrication procedure provides flexible dimensional control over such features as colloidal diameter, whole film thickness, and TiO_2 frame thickness. Unlike conventional sol–gel-based TiO_2 preparation, the use of non-aggregated monodisperse TiO_2 nanoparticles enables dense packing within the interstitial volume of colloidal arrays, and consequently, minimizes shrinkage-induced cracking of the IO structure on the substrate. In this study, the performance of IO structures

[*] Dr. H. Lee, E. S. Kwak, Dr. N.-G. Park, Dr. J. Kim
Material Science Division
Korea Institute of Science and Technology
39-1 Hawolgok-dong Seongbuk-gu Seoul, 130-650 (Korea)
E-mail: lhj0630@kist.re.kr
Prof. W. Lee
Department of Chemistry, Sejong University
98 Gunja-dong, Gwangjin-gu, Seoul, 143-747 (Korea)

DOI: 10.1002/adfm.200801540

provided by non-aggregated TiO_2 nanoparticles are examined for use as a photoelectrode for DSSCs.

2. Results and Discussion

2.1. Fabrication of Inverse-Opal Structure

The schematic diagram in Figure 1 illustrates the experimental procedure for fabricating the DSSCs used in this study. An inverse-opal structure was produced using a self assembly of a 3D polystyrene (PS) colloidal array as the sacrificial template and an infiltration of organic-layer-coated TiO_2 nanoparticles as the photovoltaic material. The use of organic-layer-coated TiO_2 nanoparticles has several advantages over sol–gel methods. First, the existence of an organic layer (i.e., acetylacetonato ligand) on TiO_2 nanoparticles produces a non-aggregated transparent TiO_2 solution in butanol, as shown in Figure 2, which consequently results in high-density packing within the interstitial volumes between the PS particles. Second, the use of highly crystalline nanoparticles minimizes the volume contraction that occurs during the removal of a sacrificial polymer (PS beads) template by thermal decomposition. Such a non-aggregated transparent TiO_2 solution can even form multilayer structures of TiO_2 films of optical quality.[41] The crystallinity of the TiO_2 particles was revealed as anatase by X-ray diffraction (XRD) and transmission electron microscopy (TEM) analysis. Figure 2a shows the typical XRD patterns recorded for the TiO_2 nanoparticles. Several characteristic diffraction peaks corresponding to anatase (101), (200), and (105) morphology show up at $2\theta = 25.2^\circ$, 37.1°, and 48°, respectively. Based on the Scherrer equation, an average grain size of 15 Å was calculated from the peak broadening of the XRD pattern.[42] These values are consistent with the mean sizes observed by high-resolution transmission electron microscopy (HRTEM) experiments which show the lattice planes of crystalline nanoparticles with a diameter of approximately 40 Å (see Fig. 2b). Lattice images of 2.67 Å and 3.55 Å are clearly observable, corresponding to the {110} and {101} planes of the TiO_2 anatase phase, respectively.

Figure 3 shows scanning electron microscope (SEM) images of the PS colloidal structures. The films consisted of a 12-μm-thick structure of PS colloids of which the diameters were 1 000 nm, 400 nm, and 240 nm, respectively, and exhibited a dense face-centered cubic (fcc) structure. These structures were composed of grains that were approximately 20–100 micrometers in length and aligned in multiple directions. After calcination, an IO structure with ordered cavities was successfully generated, as shown in Figure 4. Compared to the original sizes of the PS microspheres, the diameters of the spherical voids were decreased by 10%. This volume contraction was much less serious than in the IO structures of the control experiment which was formed by the direct sol–gel hydrolysis of metal-organic alkoxide precursors within the opal structure. To compare the effect of the calcination process using the non-aggregated titania particles and typical sol–gel-driven titania materials, thermal gravimetric analysis (TGA) was performed to measure the weight loss of materials as a function of temperature. It was found that the authors' titania nanoparticles showed an approximate 25% weight loss at 350 °C; whereas the typical sol–gel method showed an exceptionally large weight loss (approximately 85%) at a similar temperature. Consequently, the latter titania would produce a large volume contraction and low cell performance.[29,32] Therefore, the use of non-aggregated nanoparticles was confirmed to induce a compact inverse-opal structure over the whole cell area, overcoming the disadvantages of the sol–gel method.

The formation of high-quality colloidal crystal templates would result in optical diffraction at wavelengths relative to the sphere (or cavity) size or refractive index of the materials. The position of reflectance peaks in fcc photonic crystals can be considered using Bragg's law, which takes into account the refraction of light in the composite structure and the incident angle of the incoming light.[37] Using the modified Bragg's law for normal incidence as shown in Equation 1, the refractive index of TiO_2 can be estimated using a measured value of a reflection peak, λ_p,

$$\lambda_p = 2d_{hkl}\sqrt{n_s^2 f + n_f^2(1-f)} \quad (1)$$

where λ_p is the maximum wavelength of the reflected peak (the position of the photonic bandgap), d_{hkl} is the interplanar spacing between *hkl* planes, n_s is the refractive index of the spheres, and n_f is the refractive index of the framework. In first-order Bragg diffraction from fcc (111) planes, $d_{hkl} = 0.8165D$, where D is the average center-to-center distance between hexagonally packed layers on the (111) planes; f_s and f_f are the volume fractions occupied by spheres and the solid framework (TiO_2) in the structure, which are generally taken as 74% and

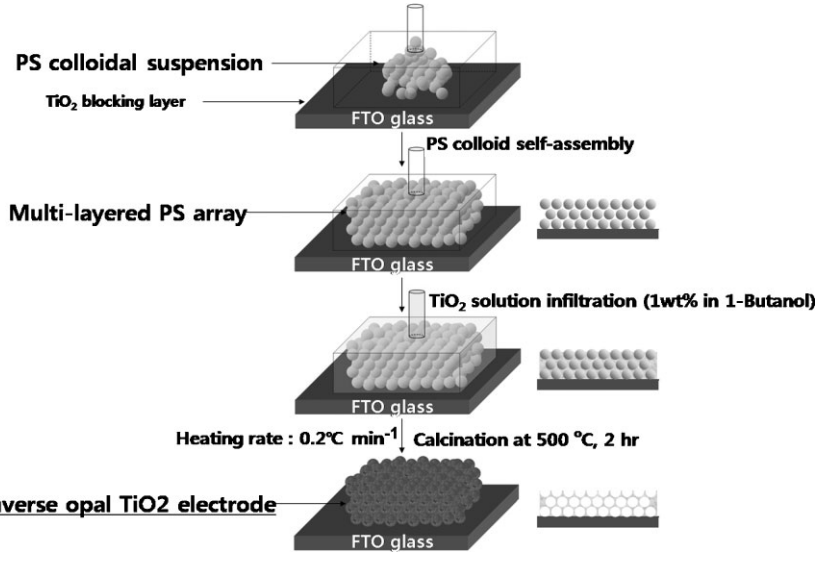

Figure 1. Schematic diagram showing the preparation steps of the 3D colloidal-array-templated TiO_2 electrode.

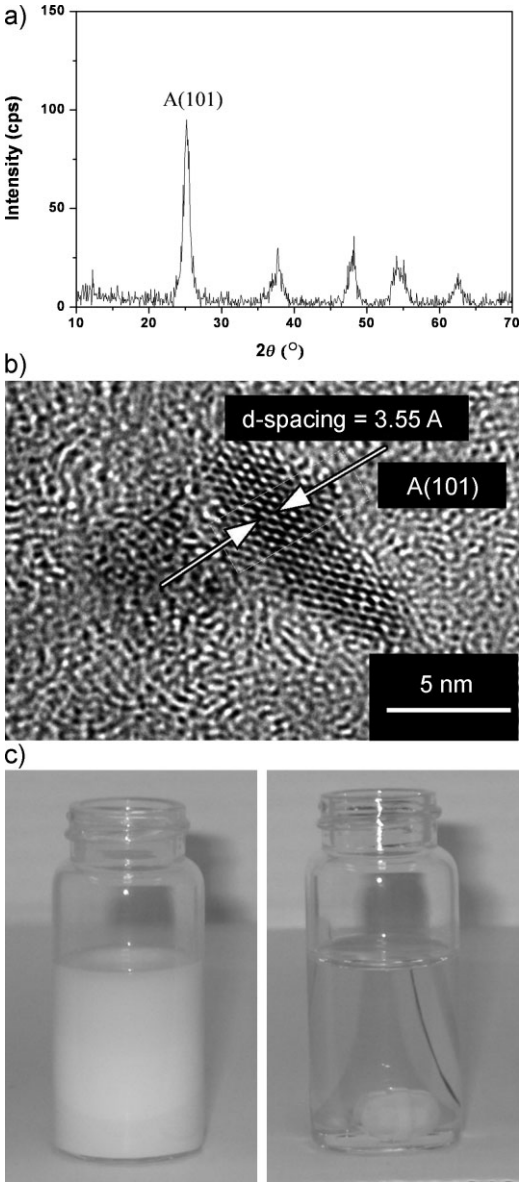

Figure 2. Characterizations of TiO_2 particles: a) XRD patterns of theTiO_2 sample used in this study after heating at 500 °C. b) TEM images of anatase TiO_2 nanoparticles. c) Optical images of a conventional TiO_2 dispersion (left) and the transparent TiO_2 nanoparticles used in this study (right).

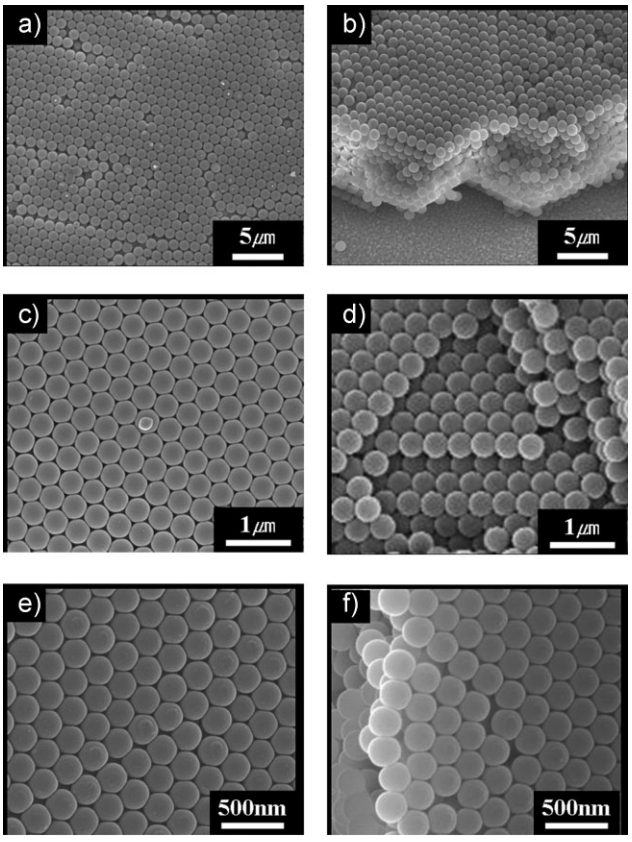

Figure 3. SEM images of colloidal photonic crystals from a, b) 1 000-nm, c, d) 400-nm, and e, f) 240-nm polystyrene (PS) microspheres, respectively.

26%, respectively, for a fcc lattice. Figure 5 shows the typical reflectance spectrum for 400-nm PS colloid particles at each of the stages displayed in Figure 1. The PS colloidal array showed a reflection peak (λ_p) at 822 nm and the diameter of the PS spheres was calculated as 345 nm using Bragg's law (Equation 1). After TiO_2 infiltration, λ_p shifted to a longer wavelength (854 nm) due to the higher refractive index of the TiO_2 nanoparticles. As revealed by the XRD experiments, the crystalline phase changed to anatase, the refractive index of which is 2.4–2.5. After thermal calcination and infilling the inverse-opal structures with the liquid electrolytes used in DSSCs, λ_p appeared at 675 nm. Applying Bragg's law again, the refractive index of the TiO_2 framework was calculated as 2.2 using the maximum reflection peak position (854 nm), the diameter of the PS spheres (345 nm), and an average refractive index of electrolyte of 1.445. Several independent measurements showed the refractive-index values of TiO_2 in this study to be in the range of 2.2–2.3. The slightly lower refractive-index value indicates the existence of polycrystalline domains within the TiO_2 particles or insufficient filling of nanoparticles.

A colloidal-template approach provides a simple and versatile way to produce inverse-opal structures having a high packing efficiency with the ability to control parameters such as cavity diameter and film thickness. The holes between neighboring cavities are caused by the necking of spheres in the fcc packing and are revealed by templating followed by calcination; these holes make the titania framework and cavities interconnected. This interconnected inverse-opal structure provides multiple beneficial effects. The electrolytes can easily be infiltrated down to the fluorine-doped tin-oxide-coated (FTO) glass due to the wide, interconnected pores of the IO structure. The mesoporous structure facilitates the infiltration of quasi-solid state or solid state electrolytes such as polymer gels, ionic liquids or hole-transport materials. Another possible benefit is the enhancement of light intensity in a certain wavelength range, obtained through controlling the colloidal diameters, due to the large scattering

spherical voids[43] and additional photonic band gap properties;[30–32,44] this issue is not within the scope of the current investigation.

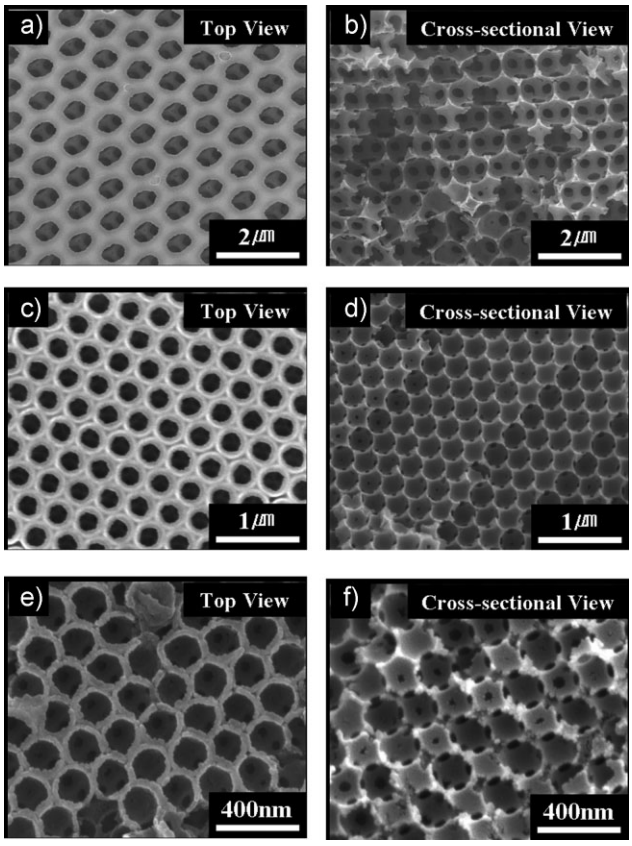

Figure 4. SEM images of the templated inverse-opal TiO_2 films showing well-formed inverse-opal structures. a, b) from 1,000-nm PS, c, d) from 400-nm PS, and e,f) 240-nm PS microspheres. The three black spots within the hexagons indicated in (b) show the holes connecting the spherical cavities to the inner layer.

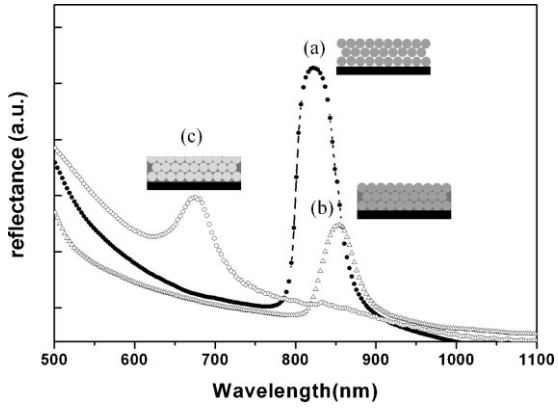

Figure 5. Reflectance spectra of the a) 400-nm PS colloidal array, b) TiO_2-nanoparticle-infiltrated PS colloidal array, and c) liquid-electrolyte-infiltrated TiO_2 inverse-opal structure.

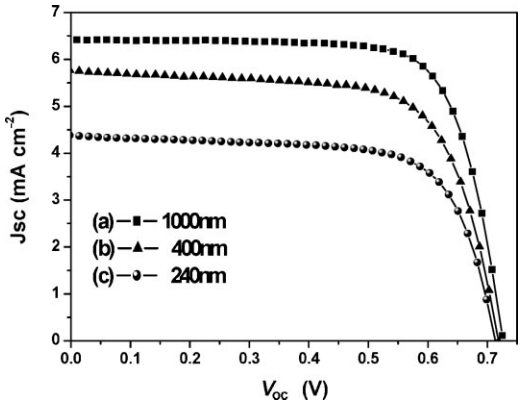

Figure 6. Current-density–voltage characteristics of three inverse-opal cells made from different sized PS templates, measured at AM 1.5 (100 mW cm^{-2}) illumination.

2.2. Solar-Cell Performance

DSSC structures were assembled with colloidal-array-templated TiO_2 photoelectrodes with three different sizes of PS beads at an illumination intensity of air mass 1.5. Their photocurrent density–voltage characteristics are shown in Figure 6, and the related physical values such as η (light-to-electricity conversion efficiency), J_{sc} (short-circuit current), V_{oc} (open circuit voltage), and *FF* (fill factor) are summarized in Table 1. The light-to-electricity conversion efficiency of solar cells, η, can be evaluated from the equation

$$\eta = (FF \times |J_{SC}| \times V_{OC})/P_{in} \quad (2)$$

where *FF* is the fill factor, $|J_{sc}|$ is the short circuit current, V_{oc} is the open circuit voltage, and P_{in} is the incident light power density. The conversion efficiency was found to increase from 2.18% for a 240-nm-diameter PS-templated cell to 2.86% for a 400-nm-diameter PS-templated cell and 3.47% for a 1 000-nm-diameter PS-templated cell. The total film thickness was fixed at 12 μm. In previous reports based on sol–gel TiO_2 infiltration, volume contraction caused serious problems in cell performance and the resultant cell efficiencies were far below a practical value (<0.6%)

Table 1. Photocurrent–voltage characteristics of inverse-opal TiO_2 solar cells [a].

Pore size – Electrode thickness	Area(cm^2)	V_{oc} (V)	J_{sc} (mA cm^{-2})	*FF*	η(%)
(a) 1–12 μm	0.170	0.726	6.42	74.4	3.47
(b) 400 nm–12 μm	0.250	0.719	5.77	69.0	2.86
(c) 240 nm–12 μm	0.151	0.713	4.38	69.9	2.18

[a] Radiant power: 100 mW cm^{-2} (AM 1.5). Redox electrolyte: 1-butyl-3-methylimidazolium iodide (BMII), iodine (I_2), guanidium thiocyanate (GSCN), 4-*tert*-butylpyridine (TBP), acetonitrile (ACN), valeronitrile (VN).

in spite of the light-enhancement effect of the photonic bandgap.[28,29,33] Several studies have focused only on the modification of the dye adsorption spectrum within IO structures without the fabrication of DSSCs.[30–32] The cell efficiencies obtained in this study were quite high for an IO-structured electrode; this can be attributed to the compact IO electrode using non-aggregated TiO_2 nanoparticles. If IO film is assumed to have a perfect fcc packing structure, the volume fractions occupied by the PS spheres and air should be 74% and 26%, respectively. Considering that the weight fraction of TiO_2 in conventional TiO_2 paste (Solartronix Inc.) is more than 70%, the amount of TiO_2 incorporated in the cells of this study is only about one third of the typical weight, which is why these cell efficiencies are still lower than that of a typical DSSC with Solaronix paste.

The enhancement of cell efficiency with the increase of the pore diameter was examined. Both J_{sc} and V_{oc} increase as the diameter increases. In order to explain this behavior, there are two factors that should be considered; the total surface area of the porous structure and the volume filling ratio. As the pore size increases, pore volume remains constant while total surface area gets smaller,which should act against the efficiency. However, the wall thickness of IO structures, which had been interstitial volume before TiO_2 infilling, is thicker, so that the contact between the substrate and the bottom of the TiO_2 IO structure may be more intact. Furthermore, spacious interstitial room allows a more compact packing of TiO_2 nanoparticles via easy infiltration. One can imagine that the TiO_2 walls made inside a smaller PS bead are much more fragile during the fabrication process since they are thin and less dense. These effects should have compensated for the decrease of dye adsorption on the TiO_2 nanoparticles (surface area) in terms of overall cell efficiency. In DSSCs of small pores (240-nm-diameter PS-templated cells), however, conversion efficiency exhibited marked enhancement, up to 3.9% after $TiCl_4$ post-treatment. Conversely, DSSCs with large pores (1 000-nm-diameter PS-templated cells) showed only a slight increase, up to 3.6% by the same treatment. These results support that the post-treatment resolves the poor interfacial contact between the TiO_2 IO structure and the electrode and insufficient nanoparticle filling in small pores, leading to a substantial improvement in cell efficiency.

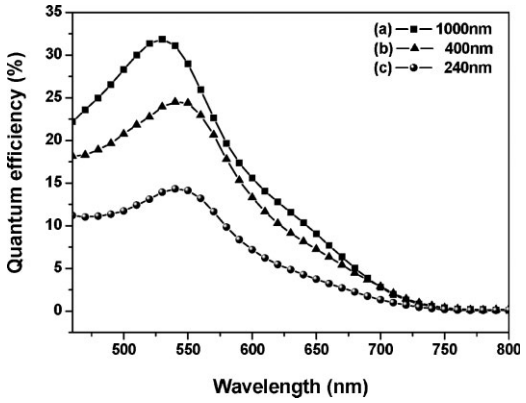

Figure 7. Incident photon to current conversion efficiency (IPCE) curves for three inverse-opal cells made from different sized PS templates.

with the maximum absorption wavelength of N719 dyes. In the case of 1 000-nm particles, the wavelength of maximum quantum efficiency was slightly blueshifted, which might be due to the existence of the higher-order stop band in TiO_2 photonic crystals. The broad absorption below 400 nm was contributed by light absorption in TiO_2. As the colloidal particles increased in size from 240 nm to 1 000 nm, the conversion efficiency increased up to 300% in the TiO_2 electrode. This behavior was supported by the electrochemical impedance analysis shown in Figure 8. The electrochemical impedance analysis was applied to investigate the interfacial characteristics of DSSCs, measuring the current response to a modulation of an applied bias. The first peak in the high frequency range (>0.1 MHz) in Figure 8 is primarily related to the sheet resistance (R_h) of FTO and remains nearly constant regardless of pore size. The largest semicircles in the low frequency range (1–10^3 Hz) represent the impedance associated with the charge transfer between the dye-sensitized TiO_2/dye/redox(I^-/I_3^-) interface (Z_1) and the Pt/redox(I^-/I_3^-) interface (Z_2).[45] As the pore size is increasing, these impedance components are supposed to be reduced because of the compact packing of the TiO_2 nanoparticles and an enhanced adhesion between TiO_2 and the blocking layer on the FTO substrate, which means the efficient electron drift mobility through the TiO_2 electrode. The diameter of the large semicircular arcs (Z_2) was also observed to decrease with an increase in the pore size. Also,

2.3. Incident Photon-to-Electron Conversion Efficiency (IPCE) and Electrochemical Impedance Analysis

To investigate the characteristics of these colloid-array-templated TiO_2 electrodes, incident photon-to-electron conversion efficiency (IPCE) and electrochemical impedance analysis were performed for three IO-structured electrodes of different colloidal sizes. The IPCE is defined as the number of generated electrons divided by the number of incident photons. The IPCE spectra in Figure 7 shows that the maximum efficiency is located around 540 nm, which coincides

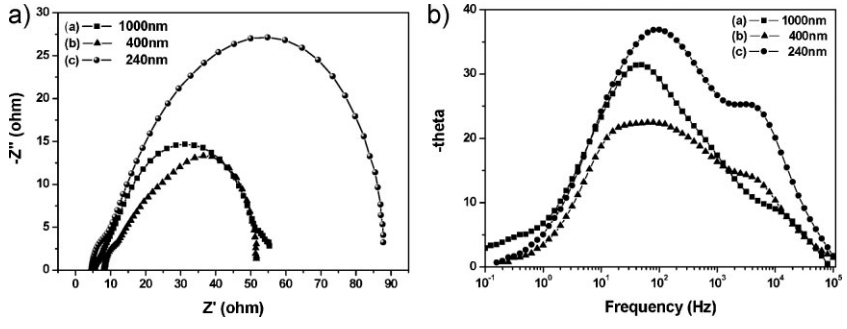

Figure 8. Impedance spectra of three inverse-opal cells made from different sized PS templates. a) Bode phase plots. b) Nyquist plots.

the ω_{max} values of the arc (Z_2) slightly decreased as the pore size increased, as shown in Figure 8b. (from ~20 Hz to ~12 Hz) These values are similar to those of the nanoparticle-based cells (~15 Hz) reported previously.[40] In general, the ω_{max} value reflects the lifetime of electrons for recombination τ_r at the TiO_2/electrolyte interface, and consequently, a decrease in the ω_{max} value means slower recombination. While the photoinjected electrons traverse the interconnecting network of TiO_2 to the charge-collecting FTO substrate, they undergo recombination reactions with a time constant (τ_r) at the TiO_2/electrolyte interface. Thus, as slower recombination occurs, more electrons are collected. This indicates that IO film with large pores is more favorable than that with small pores for the reduction of recombination processes.

As seen from the IPCE results and the electrochemical impedance measurements, the IO structure constructed from large PS particles has more efficient cell performance. As mentioned above, the experimental observations could be attributed to a more compact packing of TiO_2 through a larger interstitial space, which ensures i) intact interfacial contact between the blocking layer and the bottom of the IO structure to minimize the contact resistance at the junction, ii) facile electron transport throughout the interconnected TiO_2 IO structure, and iii) easy infiltration of the electrolyte through the wider interconnected pores.

3. Conclusions

Compact and ordered TiO_2 inverse-opal photoelectrodes were prepared using a 3D colloidal-array templating route with flexible dimensional control of pore size for dye-sensitized solar-cell applications. Organic-layer-coated TiO_2 nanoparticles improved the degree of infiltration and, consequently, minimized the volume contraction during thermal calcinations of the colloidal template within the IO structure. This compact IO photoelectrode resulted in an enhanced photo-conversion efficiency of 3.47% under air mass 1.5 illumination which is more than five times greater than that reported previously for photoelectrodes based on sol–gel TiO_2 infiltration. The novel fabrication method of the IO-structured photoelectrode developed in this study is expected to create new opportunities for further light enhancement via photonic-bandgap engineering by the variation of colloidal template diameter and by shifting the absorption wavelength of the photosensitizer in photovoltaic and photoelectrochemical cells.

4. Experimental

Materials: PS microspheres (Alfa Aesar) and (tridecafluoro-1,1,2,2-tetrahydrooctyl) methyldichlorosilane (Gelest) were used without further purification. 1-butyl-3-methylimidazolium iodide (BMII, Aldrich), iodine (I_2, Aldrich), 4-*tert*-butylpyridine (Aldrich), guanidium thiocyanate (Aldrich), and ruthenium dye (*cis*-bis(isothiocyanato)-bis(2,2′-bipyridyl-4,4′-dicarboxylato) ruthenium(II) bis (tetrabutylammonium) (N719; Solaronix) were used as purchased. FTO glass substrates (TEC-8, Pilkington) were used as the transparent conducting electrode for all devices described in this paper.

Preparation of a Solar Cell Module: The procedures for solar cell device preparation are schematized in Figure 1. A thin compact layer of TiO_2 (~40 nm) was coated onto FTO glass by spin coating Ti(IV) bis(ethyl acetonato)-diisopropoxide solution (sol–gel hydrolysis) and then was calcined to 450 °C, which prevented the direct contact of the electrolytes with the FTO glass. Large-area 3D colloidal crystals of PS beads were prepared following the flow-field-induced self-assembly method described by Xia et al. [46]. This is a simple and controllable method for fabricating large-area opals with a specific film thickness. These films were annealed in air for 2 h at 80 °C to remove the water and to promote necking of the spheres, which provides the structural stability of the opal. Subsequently, TiO_2 nanoparticles were infiltrated into the interstitial volumes of these PS colloidal film. The synthesis of TiO_2 nanoparticles is described elsewhere [40]. The film was then calcined in air at 500 °C for 2 h with a slow heating rate (0.2 °C min^{-1}) in order to remove the PS beads, leaving behind air cavities in the titania matrix. The thickness of the TiO_2 film used in this work was controlled at 12 μm over a 20 mm × 20 mm area. The IO TiO_2 films on FTO glass were immersed for one day in an ethanol solution containing 0.5 mM of purified N719 dye. The dye-adsorbed TiO_2 electrodes were rinsed with ethanol and dried. A Pt counter-electrode was prepared by spin-coating H_2PtCl_6 solution (0.7 mM in isopropyl alcohol) onto the FTO glass; this was then sintered at 400 °C for 20 min. The dye-absorbed electrode and the counter electrode were assembled using 25-μm-thick surlyn sheet (DuPont 1702) as a spacer. The liquid electrolytes used here consisted of 0.7 M 1-butyl-3-methylimidazolium iodide (BMII), 0.03 M Iodine (I_2), 0.1 M Guanidium thiocyanate (GSCN), and 0.5 M 4-*tert*-butylpyridine (TBP) in a mixture of acetonitrile (ACN) and valeronitrile (VN) (85:15 v/v).

Chemical Treatment with $TiCl_4$: Before immersion in dye solution, the TiO_2 film was impregnated with a 0.2 M $TiCl_4$ aqueous solution at 30 °C for 2 h. Then, it was calcined at 450 °C in air for 30 min and allowed to cool to room temperature. The heating rate for the calcination steps was 3.5 °C min^{-1}. The following procedures adopted the typical method, as described above.

Characterization: Morphology of the synthetic opals and inverse-opal TiO_2 films was investigated using a field-emission scanning electron microscope (FESEM; Hitachi S4100). XRD data were obtained in order to confirm the crystalline structures of the TiO_2 nanoparticles. The reflectance peaks in photonic crystals were accomplished through a UV–vis–NIR spectrophotometer (JASCO V-670). TGA experiments (TA instruments) were performed under air with a solution of titanium tetraisopropoxide in ethanol and a solution of the titanium nanoparticles that were used in this study dispersed in butanol. To reproduce a similar physical condition right before calcination, solutions were dried in air for at least one day. Photocurrent–voltage measurements were performed using a Keithley model 2400 source measuring unit. A 1000-W Xenon lamp (Spectra-Physics) served as the light source and its light intensity was adjusted using a NREL-calibrated Si solar cell equipped with a KG-5 filter for approximating AM 1.5 G one-sun light intensity. IPCE was measured as a function of wavelength from 400 nm to 800 nm using a specially designed IPCE system for dye-sensitized solar cells (PV Measurement, Inc.). A 75-W xenon lamp was used as the light source for generating a monochromatic beam. Calibration was performed using a silicon photodiode (NIST-calibrated photodiode G425) as a standard, and IPCE values were collected at a low chopping speed of 10 Hz. Electrochemical impedance spectra were measured by a frequency response analyzer (Solartron, SI 1260) connected with a potentiostat (Solartron 1287) at an amplitude of 10 mV at the open-circuit voltage (V_{oc}) under 100 mW cm^{-2} illumination.

Acknowledgements

The authors thank Ms. Minah Kim for the TGA measurement. We acknowledge financial support of this work by KIST internal project and Korea research council of Fundamental Science and Technology. W. Lee acknowledges financial support by the faculty research fund of Sejong University in 2007.

Received: October 14, 2008
Published online: February 25, 2009

[1] B. O'Regan, M. Grätzel, *Nature* **1991**, *353*, 737.
[2] P. Wang, S. M. Zakeeruddin, J. E. Moser, M. K. Nazeeruddin, T. Sekiguchi, M. Grätzel, *Nat. Mater.* **2003**, *2*, 498.
[3] M. J. Cass, A. B. Walker, D. Martinez, L. M. Peter, *J. Phys. Chem. B* **2005**, *109*, 5100.
[4] N. H. Damrauer, G. Cerullo, A. Yeh, T. R. Boussie, C. V. Shank, J. K. McCusker, *Science* **1997**, *275*, 54.
[5] J. Bisquert, D. Cahen, G. Hodes, S. Ruhle, A. Zaban, *J. Phys. Chem. B* **2004**, *108*, 8106.
[6] J. H. Yoon, S. R. Jang, R. Vittal, J. Lee, K. J. Kim, *J. Photochem. Photobiol. A* **2006**, *180*, 184.
[7] M. Paulose, K. Shankar, O. K. Varghese, G. K. Mor, C. A. Grimes, *J. Phys. D* **2006**, *39*, 2498.
[8] G. K. Mor, K. Shankar, M. Paulose, O. K. Varghese, C. A. Grimes, *Nano Lett.* **2006**, *6*, 215.
[9] J. T. Jiu, S. Isoda, F. M. Wang, M. Adachi, *J. Phys. Chem. B* **2006**, *110*, 2087.
[10] Y. Ohsaki, N. Masaki, T. Kitamura, Y. Wada, T. Okamoto, T. Sekino, K. Niihara, S. Yanagida, *Phys. Chem. Chem. Phys.* **2005**, *7*, 4157.
[11] J. B. Baxter, E. S. Aydil, *Appl. Phys. Lett.* **2005**, *86*.
[12] N. Kopidakis, K. D. Benkstein, J. van de Lagemaat, A. J. Frank, Q. Yuan, E. A. Schiff, *Phys. Rev. B* **2006**, *73*, 045326.
[13] P. E. deJongh, D. Vanmaekelbergh, *Phys. Rev. Lett.* **1996**, *77*, 3427.
[14] J. Nelson, S. A. Haque, D. R. Klug, J. R. Durrant, *Phys. Rev. B* **2001**, 6320.
[15] M. Guo, P. Diao, X. D. Wang, S. M. Cai, *J. Solid State Chem.* **2005**, *178*, 3210.
[16] Y. Gao, M. Nagai, *Langmuir* **2006**, *22*, 3936.
[17] N. Nang Dinh, M.-C. Bernard, A. Hugot-Le Goff, T. Stergiopoulos, P. Falaras, *C. R. Chim.* **2006**, *9*, 676.
[18] F. Lenzmann, J. Krueger, S. Burnside, K. Brooks, M. Grätzel, D. Gal, S. Ruhle, D. Cahen, *J. Phys. Chem. B* **2001**, *105*, 6347.
[19] E. Hosono, S. Fujihara, I. Honna, H. S. Zhou, *Adv. Mater.* **2005**, *17*, 2091.
[20] M. Fu, J. Zhou, Q. F. Xiao, B. Li, R. L. Zong, W. Chen, J. Zhang, *Adv. Mater.* **2006**, *18*, 1001.
[21] G. Duan, W. Cai, Y. Luo, F. Sun, *Adv. Funct. Mater.* **2007**, *17*, 644.
[22] Y. Diamant, S. Chappel, S. G. Chen, O. Melamed, A. Zaban, *Coord. Chem. Rev.* **2004**, *248*, 1271.
[23] N. G. Park, M. G. Kang, K. M. Kim, K. S. Ryu, S. H. Chang, D. K. Kim, J. van de Lagemaat, K. D. Benkstein, A. J. Frank, *Langmuir* **2004**, *20*, 4246.
[24] M. Law, L. E. Greene, J. C. Johnson, R. Saykally, P. D. Yang, *Nat. Mater.* **2005**, *4*, 455.
[25] S. Pavasupree, Y. Suzuki, S. Pivsa-Art, S. Yoshikawa, *Sci. Technol. Adv. Mater.* **2005**, *6*, 224.
[26] W. U. Huynh, J. J. Dittmer, A. P. Alivisatos, *Science* **2002**, *295*, 2425.
[27] A. Mihi, H. Miguez, *J. Phys. Chem. B* **2005**, *109*, 15968.
[28] C. L. Huisman, J. Schoonman, A. Goossens, *Sol. Energy Mater. Sol. Cells* **2005**, *85*, 115.
[29] P. R. Somani, C. Dionigi, M. Murgia, D. Palles, P. Nozar, G. Ruani, *Sol. Energy Mater. Sol. Cells* **2005**, *87*, 513.
[30] S. Nishimura, N. Abrams, B. A. Lewis, L. I. Halaoui, T. E. Mallouk, K. D. Benkstein, J. van de Lagemaat, A. J. Frank, *J. Am. Chem. Soc.* **2003**, *125*, 6306.
[31] L. I. Halaoui, N. M. Abrams, T. E. Mallouk, *J. Phys. Chem. B* **2005**, *109*, 6334.
[32] A. Mihi, L.-A. F.J. López-Alcaraz, H. Míguez, *Appl. Phys. Lett.* **2006**, *88*, 193110.
[33] A. Mihi, M. E. Calvo, J. A. Anta, H. Miguez, *J. Phys. Chem. C* **2008**, *112*, 13.
[34] O. D. Velev, E. W. Kaler, *Adv. Mater.* **2000**, *12*, 531.
[35] G. Subramania, K. Constant, R. Biswas, M. M. Sigalas, K. M. Ho, *J. Lightwave Technol.* **1999**, *17*, 1970.
[36] G. Subramania, K. Constant, R. Biswas, M. M. Sigalas, K. M. Ho, *Synth. Met.* **2001**, *116*, 445.
[37] S. Nishimura, A. Shishido, N. Abrams, T. E. Mallouk, *Appl. Phys. Lett.* **2002**, *81*, 4532.
[38] G. Oye, W. R. Glomm, T. Vralstad, S. Volden, H. Magnusson, M. Stocker, J. Sjoblom, *Adv. Colloid Interface Sci.* **2006**, *123*, 17.
[39] M. L. K. Hoa, M. H. Lu, Y. Zhang, *Adv. Colloid Interface Sci.* **2006**, *121*, 9.
[40] E. Scolan, C. Sanchez, *Chem. Mater.* **1998**, *10*, 3217.
[41] J. Yoon, W. Lee, J. M. Caruge, M. Bawendi, E. L. Thomas, S. Kooi, P. N. Prasad, *Appl. Phys. Lett.* **2006**, *88*.
[42] M. M. Gomez, J. Lu, J. L. Solis, E. Olsson, A. Hagfeldt, C. G. Granqvist, *J. Phys. Chem. B* **2000**, *104*, 8712.
[43] S. Hore, P. Nitz, C. Vetter, C. Prahl, M. Niggemann, R. Kern, *Chem. Commun.* **2005**, 2011.
[44] E. S. Kwak, M. A. Kim, W. Lee, H. Lee, unpublished.
[45] H. W. Han, X. Z. Zhao, J. Liu, *J. Electrochem. Soc.* **2005**, *152*, A164.
[46] S. H. Park, B. Gates, Y. N. Xia, *Adv. Mater.* **1999**, *11*, 462.